Fast Detection of Biomolecules in Diffusion-Limited Regime Using Micromechanical Pillars

Mauro Melli,[†] Giacinto Scoles,[‡,§] and Marco Lazzarino[†,*]

[†]CNR-IOM, Laboratorio TASC—Area Science Park Basovizza—ss 14 km 163.5 34149 Trieste, Italy, [‡]Synchrotron-Elettra Nano Innovation Laboratory (SENIL), Elettra Sincrotrone Trieste S.C.p.A, Area Science Park Basovizza—ss 14 km 163.5 34149 Trieste, Italy, and [§]Department of Biological and Medical Science, University of Udine, Ospedale della Misericordia 33100 Udine, Italy

In the past decade much effort has been dedicated to biomolecular detection to improve response sensitivity and velocity, approaching the fundamental limits imposed by physics and chemistry. Therefore new technological routes are required to satisfy the continuously increasing demand of sensitive and fast biosensors. A promising family of biosensors is represented by micro- and nanomechanical systems[1] which provides unique opportunities to measure forces, displacements, and mass changes from cellular and subcellular processes. Detection of mass in the zeptogram range[2] and sensitivity in liquid to the fraction of nM concentration in real time have been demonstrated.[3]

However a significant limitation hinders the application of ultrasensitive detecting schemes able to respond to a single molecule event. At low concentration, typical of biomolecular experiments, the transport of target molecules to the sensor can play as critical a role as the chemical reaction itself[4] in governing binding rate. This aspect was in the past largely underestimated, but recently it has been gaining much more attention from the analytical community. Diffusion limitations will play a key role in the development of biosensors for protein recognition because of the extremely low concentration of analyte in practical applications, the low diffusion constants determined by the generally large size of proteins, and the lack of PCR amplification procedures analogous to those available for DNA. Several theoretical and experimental studies reporting the influence of the mass transport on antibody biosensors as a function of analyte concentration and incubation time concluded that pushing the sensitivity to the limit of single molecule detection may not bring the expected benefit to the overall performance.[5−7] In fact, mass transport can

ABSTRACT We have developed a micromechanical sensor based on vertically oriented oscillating beams, in which contrary to what is normally done (for example with oscillating cantilevers) the sensitive area is located at the free end of the oscillator. In the micropillar geometry used here, analyte adsorption is confined only to the tip of the micropillar, thus reducing the volume from which the analyte molecules must diffuse to saturate the surface to a sphere of radius more than 2 orders of magnitude smaller than the corresponding linear distance valid for adsorption on a macroscopic surface. Hence the absorption rate is 3 orders of magnitude faster than on a typical 200 × 20 square micrometer cantilever. Pillar oscillations are detected by means of an optical lever method, but the geometry is suitable for multiplexing with compact integrated detection. We demonstrate our technology by investigating the formation of a single-strand DNA self-assembled monolayer (SAM) consisting of less than 10^6 DNA molecules and by measuring their hybridization efficiency. We show that the binding rate is 1000 times faster than on a "macroscopic" surface. We also show that the hybridization of a SAM of maximum density DNA is 40% or 4 times the value reported in the literature. These results suggest that the lower values previously reported in the literature can be attributed to incomplete saturation of the surface due to the slower adsorption rate on the "macroscopic" surfaces used.

KEYWORDS: biosensor · micromechanical sensor · cantilever · DNA-oligos · DNA hybridization · diffusion limited kinetics

significantly lower the practical sensitivity of a device by reducing the number of binding events. Furthermore, the response time can increase to an unreasonable value (days or weeks) making highly sensitive devices useless.

Nanotechnology may help to tackle the challenge of increasing the sensitivity by intrinsically modulating the diffusion process. The most important example is the integration of biosensors within microfluidic systems. In fact, a proper flux of the analyte toward the sensing surface can significantly increase sensor response.[4]

On the other hand, it has been reported that the dimension and shape of a sensor affect the mass transport and the flux of molecules toward the active area.[5,6] Nair et al. reported several theoretical studies

about the performance of a biological sensor as a function of its shape and dimensionality.[5,8,9] In particular, they reported that nanowire sensors have higher sensitivity than planar sensors because the different diffusion field increases the total flux of molecules toward the surface. They estimated that the detection limit of a typical nanosized sensor is 3 to 4 orders of magnitudes higher than a planar sensor.

We have developed a micromechanical sensor based on vertically oriented oscillating beams[10,11] (or pillars) which make it possible to locate the sensitive area at the free end of the oscillators. An array of such pillars behaves as an array of isolated nanosized sensors embedded in a quasi-infinite analyte solution. While the top face of the pillars represents the nanosized active area, the pillars themselves can be operated as mass detectors. Mechanical weighing is a powerful, highly reproducible, and sensitive down to the single molecule[12] method which has been proven to quantitatively detect molecular absorption. Usually tiny cantilevers or doubly clamped bridges are excited at one of their mechanical resonances, and resonance-frequency variation upon mass adsorption is recorded. Our sensor architecture is based on inverted-tapered pillars and consists of beams protruding out of a Si wafer surface (see Figure 1A,B). A detailed description of the fabrication procedure has been published elsewhere.[11] As in cantilever sensing, the adsorption of extra mass causes a change of the resonance frequency. However, the adsorbed mass is localized exactly at the free end of the beam due to the sensor geometry and this avoids adsorption on the beam sides which may cause several spurious effects such as bending and adding of surface stress. For these properties, unlike with standard cantilevers, the pillar geometry allows a proper application of the spring model and an accurate linear dependence between the added mass and the change in frequency with the only approximation that the added mass is small respect to the total mass of the resonator. The range of resonance frequency of the devices is 5−7 MHz and the typical responsivity is 33 Hz/fg. Since we are able to determine the variation of frequency within 10 ppm we can measure the adsorption of mass of the order of 1.5 fg which corresponds to 7.0×10^5 DNA molecules or to the coverage density of 2.8×10^{11} mol/cm^2.

We arrange the pillars in a dense hexagonal array as shown in Figure 1A, contoured by a continuous corral, and we passivate the whole structure with a C_4F_8 plasma treatment in order to make all surfaces hydrophobic. The proper combination of pillar geometry and chemical termination results in a superhydophobic (or Lotus leave-like) behavior of the whole structure.[13-] According to Wenzel's model,[14] if a substrate is very hydrophobic and/or very rough (roughness is defined as the ratio of the actual over the apparent surface area), the contact angle of a liquid drop can reach
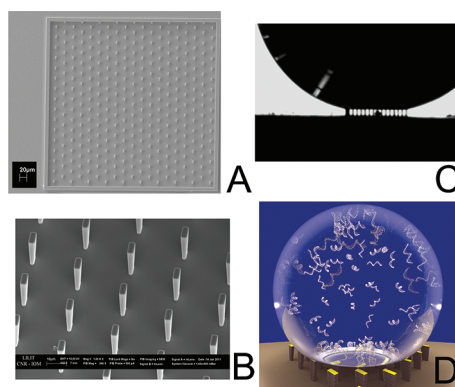

Figure 1. (A) SEM images of the devices. Note the hexagonal lattice of pillars, arranged in 19 rows of 16 pillars each. The distance between neighboring pillars is 20 μm. The structure is enclosed in a square corral of the same height of the pillars, that prevents water from wetting from the sides. The size of a single pillar is 3 μm × 8 μm in plane and 15 μm in height. (B) Tilted image of a region of the device. (C) Lateral view of a device with a water drop on top taken with a long working distance optical objective. To see the pillar matrix we fabricated devices without the square corral. The drop wets only the pillar top surfaces while air remains trapped between pillars. (D) Schematics of superhydrophobic conditions. A drop of a solution of DNA and buffer floats on top of the pillars, and the molecules can reach only the microsized area at the end of the contact pillars.

values larger than 150° (super-hydrophobic state). Moreover, by tuning the geometry of the substrate it is possible to induce the drop to be in the so-called Cassie state in which air remains trapped between the substrate and the droplet that results partially suspended.[15] It was indeed demonstrated[16] that a regular matrix of pillars may result in a super hydrophobic surface and induce a Cassie state. Droplets in Cassie regime were reported even for moderate hydrophobicity or roughness of the patterned surface.[17] We verified by imaging that the hexagonal arrays of pillars designed by us showed a super-hydrophobic behavior with the droplet sitting on the pillar top and air filling the space between pillars (see Figure 1C and Supporting Information). In this configuration only the top surface of the pillar is in contact with the analyte solution while the pillar walls are not exposed as shown in the rendering of Figure 1D. In our geometry, the absorption sites are the microsized areas defined by the top of the pillars. Since there are no other device surfaces in contact with the analyte solution, there is no aspecific absorption, and the devices can be modeled without any approximation as true micrometer sized absorbers. In contrast, with other techniques the adsorption is either on large areas, like in standard cantilevers, or the nanosized sensitive area is embedded into the larger surface of the device, as in nanowire sensors.

RESULTS

We first performed preliminary simulations by means of a commercial finite-element-method software in order to investigate the effects of the absorbing surface

size on the binding rate. To take into account both the diffusion of the analytes and the kinetics of the reaction at the surface, we coupled the equation for the surface reaction (Langmuir equation) with the mass transport in the solution (Fick's law). The coupling is given as a boundary condition of the bulk's mass balance equation. The outgoing flux of the concentration at the boundary due to adsorption is set equal to the rate of surface reaction (see the Methods section for details). The local coverage is given by the function θ_s (x,t) and follows the standard Langmuir equation:

$$\frac{\partial \theta_s}{\partial t} = C_s(t) k_{ads}(\theta_0 - \theta_s(t)) - k_{des}\theta_s$$

where k_{ads} is the rate of adsorption, k_{des} is the rate of desorption, $C_s(t)$ is the solution concentration at the adsorbing area, and θ_0 is the maximum number of binding sites per unit area. We simulated the adsorption of thiolated single-strand DNA molecules (ssDNA) with molecular weight of 12 kDa and diffusion constant of 1.0×10^{-6} cm^2/s on a large flat gold surface and on a 3 μm $\times$ 8 μm rectangular gold area which has the dimension of the pillar top (see Figure 2). We varied the kinematics parameters until we found the best set which reproduces the experimental data ($k_{ads} = 1.32 \times 10^5$ (M·s)$^{-1}$ and $k_{des} = 1.5 \times 10^{-4}$ s^{-1}). The simulations show three phases. Initially, the region near the surface is quickly depleted, a very low molecular density film is formed, and a large concentration gradient is created near the surface. Later, due to the concentration gradient, molecules far from the surface migrate toward the surface and start being adsorbed. In this second phase, molecular adsorption can be very slow and its rate is imposed by the diffusion constant. In the last phase the molecular film on the surface is almost at saturation value, there is no more adsorption, and the depletion layer re-equilibrates to the bulk concentration. Only the second phase is significantly different on the pillar and on the flat surface.

In our simulations, the saturation density of 2.1×10^{13} mol/cm^2 was reached in 1500 s on a flat surface with a solution concentration of 1 μM, while for the micrometer-sized area the same density was obtained in only 20 s. This shows that the same surface reactivity can result in a large difference of the binding rate when the diffusion field is substantially modified by the geometry and the size of the absorber.

To test the pillar sensor experimentally, we measured directly and quantitatively the formation of ssDNA self-assembled monolayers (SAMs) on gold-coated surfaces and their hybridization efficiency, defined as the ratio of hybridized DNA probes *versus* the total number of ssDNA probes, and we compared our results with the data available in literature for extended surfaces. In DNA hybridization technology, the main studies about kinetics, equilibrium of adsorption, and hybridization, were based on indirect techniques such
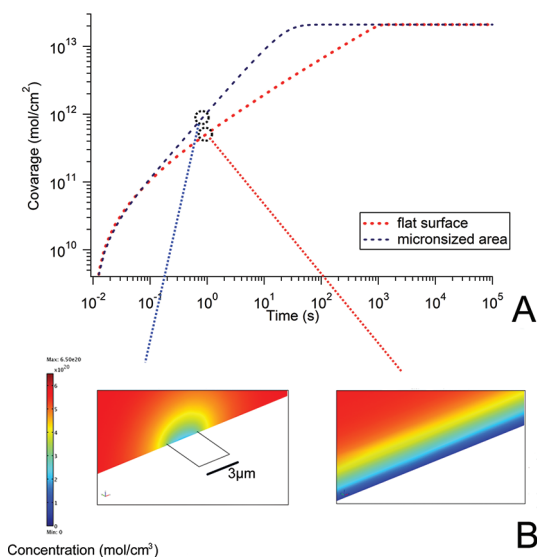

Figure 2. Results of the simulations of the adsorption onto a flat surface and onto a micrometer-sized area. (A) The coverage as a function of the incubation time on a flat surface (red dots) and on a micrometer size area (blue dots). In the initial phase, the two curves are almost overlapped because the systems are equivalent and then have different slopes until they reach the saturation due to the different influence of the diffusion. **(B)** Two snapshots that display the local concentration of molecules in solutions at increasing times for the two different geometries after 1 s. The contour plots of the concentration are shown in a plane perpendicular to the adsorbing surface. The images clearly show the differences of the concentration near the adsorbing areas. In the case of micrometer sized area, a spherical depletion region with a low gradient is formed. Conversely, a planar large gradient is produced near to an extended flat surface. The rectangle in the image on the left corresponds to 3 μm $\times$ 8 μm area of the top of the pillar. The slice plot intersects the middle of the rectangle.

as X-ray photoemission spectroscopy, radio labeling[18] or surface plasmon resonance[19,20] which require large samples and average over a large amount of molecules. One of the main widely accepted assessments is that the formation of a well formed ssDNA SAM requires many hours if not days at rather high DNA concentration and that hybridization efficiency depends strongly on probe density and slightly on the immobilization procedure.[20] In particular, in the highest density (1.2×10^{13} mol/cm^2) self-assembled monolayers of DNA molecules, the hybridization efficiency is below 10%. Fine-tuning of the SAM properties does not seem to be a valid strategy to improve the detection efficiency. However, Demers *et al.*[21] reported a hybridization efficiency of 33% of a high density (overnight immobilization) target film after an incubation of 40 h. This result suggests that the mass transport dependence of DNA hybridization process, which did actually not hinder the diffusion and use of DNA/RNA microarrays, plays an important role even if it has been overlooked in the past and there are still very few studies about it.[19,22] For example, in their theoretical work Gadgil *et al.*[22] conclude that the rate of duplex formation strongly depends on strands diffusion in solution.

The preparation of the ssDNA monolayer was done according to the two-step protocol introduced by Tarlov and co-workers.[18] We prepared solutions with different concentrations of DNA using 40-bases ssDNA oligomers. One droplet of solution, of about 30 μL in volume, was delivered on top of a pillar matrix for each DNA concentration and incubation time (the latter from 10 s to 150 min). The volume used is large enough to keep the molecule concentration unaffected by the molecular absorption on the device. To prevent the evaporation of the drop, the samples were closed in a Petri dish together with a large drop of water to maintain the atmosphere saturated with water vapor. Subsequently each sample was incubated for 1 h in 1 mM solutions of 6-mercapto-1-hexanol (MCH). MCH prevents unspecific interaction between ssDNA and gold, assisting the vertical arrangement of DNA molecules. The shifts of the resonance frequency were measured in vacuum, using an optical setup where a laser beam was focused onto a pillar surface and the reflected beam was measured by a four-quadrant photodiode (see Figure 3A for a schematic of the experimental setup and the method section for further details). Typical frequency spectra at the first mechanical resonance are displayed in Figure 3B, where the resonance frequency is shifted to progressively lower values for each mass increment. The MCH contribution is calculated by considering that the surface S_{TOT} is completely covered by DNA and MHC molecules. We assume that the areas occupied by a single molecule of ssDNA and MHC are 2.5 nm^2 (S_{DNA}) and 0.5 nm^2 (S_{MHC}), respectively. Since the mass variation m_{TOT} is also given by the sum of both contributions it is possible to define a system of linear equations whose solution gives the numbers of MCH and ssDNA molecules, N_{MCH} and N_{DNA}.

$$\begin{cases} S_{DNA}N_{DNA} + S_{MHC}N_{MHC} = S_{TOT} \\ m_{DNA}N_{DNA} + m_{MHC}N_{MHC} = m_{TOT} \end{cases}$$

Where m_{DNA} and m_{MHC} are the mass of a single molecule of DNA and MHC, respectively.

It is worth noting that the contribution of MCH is significant (>10% of the total mass) only for low density ssDNA SAM (<2 $\times$ 10^{12} mol/cm^2). The values of the coverage of DNA film are plotted in Figure 4 as a function of the incubation time for three different thiolated ssDNA concentrations. The continuous green line shows a typical experimental result on an extended surface for a 1 μM concentration.[20] Our data for the adsorption curve at the 1 μM concentration show instead a very fast adsorption. The saturation value of the probe density was reached after less than 1 min of exposure to the solution and shows a value of 2.1 $\pm$ 0.1 $\times$ 10^{13} mol/cm^2 higher than previously reported.[19,20] The black line connecting the experimental points corresponds to the output of the simulations displayed in Figure 2, and is not the result of a data fitting

procedure. The maximum probe densities for 100 nM and 10 nM, after 2.5 h of incubation, have the values 1.7 and 1.5 $\pm$ 0.1 $\times$ 10^{13} mol/cm^2, respectively. The curves approach similar saturation values although we do not have experimental evidence that saturation was reached. Therefore, assuming the surface coverage obtained at 1 μM is equal to the density of available surface binding sites, we argue that the dissociation constant (K_D) is lower than 10 nM, about 100 times lower than the only one reported in literature[23] but compatible with other indirect measurements, such as desorption time and saturation coverage, reported in other works.[18-20] Moreover the $K_D = k_{des}/k_{ads}$ resulting from our simulation, as discussed in the previous paragraph, is 1.1 nM. A precise measurement of K_D is however beyond the scope of this paper.

It is worth noting that the time required to reach a given surface coverage is about 3 orders of magnitude shorter on pillars with respect to "large" flat surfaces while approximate simulations account for a factor of 100 (see Figure 2). The model used in the simulation is indeed too simple to provide a full description of the adsorption on the pillars. For example, it neglects the bowed solution—air interfaces, where concentration gradients can show a nontrivial behavior. Moreover, buffer salinity and charge effects which can also contribute to the creation of additional gradients had not been taken into account in our simulation. A more detailed simulation which takes into account all those parameters would require a huge computational effort, without adding new insights to the main achievements described in this paper.

The final film density is twice the values reported experimentally on extended surfaces. To understand this difference we first estimate the time required to obtain saturation for an extended surface. We assume for simplicity the surface to be infinite and the sticking coefficient to be equal to 1. To saturate the surface a volume of height $h = \sigma/c$ should be depleted, where σ is the molecular surface density and c is the molecular concentration in solution. In the absence of external driving forces, the molecular transport is regulated by diffusion, and the time scale of the process is given by[24]

$$\tau_{flat} = \frac{h^2}{D} \quad h = \frac{\sigma}{c}$$

where D is the diffusion coefficient of the molecules. The resulting saturation time required for the formation of a close packed SAM of 25 base long DNA thiolated oligomers starting from a 1 μM solution is 2.25 h. In real experiments the sticking coefficient is less than 1 and not all the molecules diffuse toward the surface; thus the surface saturation is reached in much longer times and does not depend by the actual area A. This effect is observable in the data published by Georgiadis and co-workers, where the SAM molecular
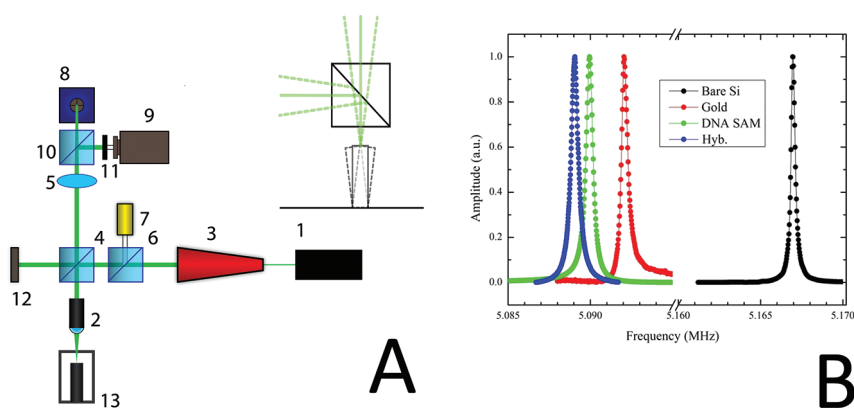
Figure 3. (A) The resonance frequency is measured by means of the optical deflection method. Scheme of the experimental set up: (1) laser, (2) microscope objective, (3) beam expander, (4) beamsplitter, (5) tube lens, (6) beamsplitter, (7) illuminator, (8) photodetector, (9) CCD camera, (10) beamsplitter, (11) long pass filter, (12) power meter, (13) chamber. The setup is built to focus a laser beam to a spot of a few micrometers, to focus the light reflected from a pillar onto a photodetector, and to visualize the laser spot and the device by means of a CCD camera. Inset. Schematics of the principle of detection. The top of the pillar acts as a tilting mirror. (B) Normalized resonance curves of a pillar after each experimental step, that is, bare silicon (starting condition), gold coating, DNA + MCH SAM, hybridization. The frequency axis is interrupted in order to accommodate the large shift due to gold deposition and the much smaller shift due to molecular absorption.
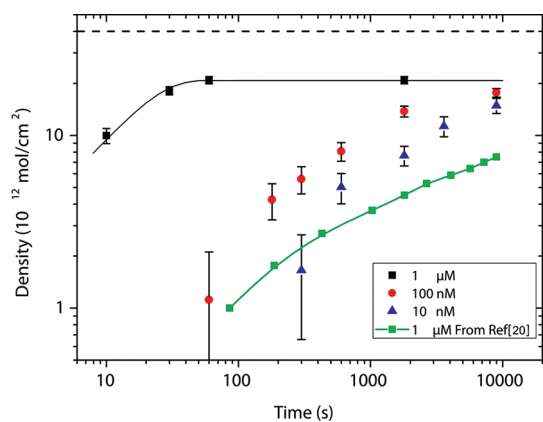

Figure 4. Immobilization rate from 10 nM, 100 nM, 1 μM ssDNA-C_6—SH solutions in 1 M NaCl TE buffer. The area of the sensor is 24 μm^2. A density of 10^{12} mol/cm^2 corresponds to 2.4 × 10^5 molecules. Green squares: kinetics of adsorption curve of 1 μM ssDNA-C_6—SH solution on a gold large surface, measured by means of SPR by Peterson *et al.* (adapted from ref 20). The dashed lines indicate the close-packed densities[31] of ssDNA SAM 4 × 10^{13} mol/cm^2. The error bar of each point represents the standard deviation on three or more pillar measurements.

Figure 5. Target hybridization rate after 1 h incubation with 1 μM cDNA solution as a function of probe density. Three different concentrations are used to prepare the ssDNA probe SAM, with no significant differences. Inset: hybridization *versus* time. The probe density is around 2 × 10^{13} mol/cm^2 and the target concentrations are 100 nM and 1 μM. The error bar of each point represents the standard deviation of three or more pillar measurements.

density is still increasing with time after 2.5 h[20] and after 5 h,[19] respectively.

Conversely, if the linear dimension of the adsorbing area (proportional to $\sqrt{A}$) is smaller than the depletion length, after an initial transient of few seconds, the process is dominated by a spherical diffusion field, and target molecules from a spherical region around the probe surface contribute to the process giving a much shorter saturation time. Our experiments demonstrate that saturation is reached well before $^1/_2$ h of incubation.

We investigated whether the dramatic change in the SAM formation rate also affects the ssDNA-SAM hybridization efficiency. We measured the hybridization of the ssDNA-SAM as a function of SAM density, by
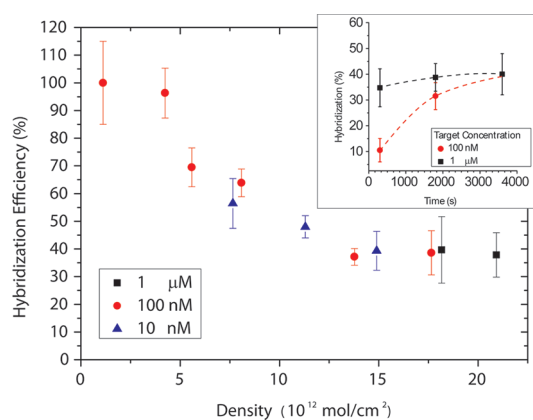
incubating the samples in a solution with the complementary sequence at 1 μM concentration for 1 h, in the same conditions used by Georgiadis and co-workers.[20] In Figure 5 we plot the hybridization efficiency, *versus* ssDNA coverage for SAMs formed from three different concentrations. We first observe that the hybridization efficiency decreases with increasing SAM density: an analogous behavior was reported in ref 20 and was attributed to repulsive electrostatic and steric interactions between neighboring molecules. Second, we observe that the only relevant parameter is the SAM surface density regardless of the preparation procedures. Thus SAMs formed in a few minutes and intrinsically more disordered show, within the experimental error, the same efficiency as SAMs formed with incubation

times of the order of several hours. Third the hybridization efficiency at the maximum ssDNA surface density (above 1.4×10^{13} mol/cm^2) has a value as high as 40%, two to four times higher than values reported in the literature.[20] As we already discussed, the reaction is strongly diffusion-limited, and in standard systems (flat surface detectors) the saturation value could require days to weeks to be achieved. To prove that in this case we reached the saturation regime, we performed hybridization experiments with shorter incubation times and lower target concentrations using the highest available probe density. The results are displayed in the inset of Figure 5 for target concentrations of 100 nM and 1 μM, and incubation times of 5 min and 30 min. Hybridization efficiency increases with incubation time and with target concentration approaching the 40% value obtained in the previous experiment. Although not a direct measure of the saturation value these data demonstrate that hybridization efficiency depends on the incubation time. We conclude that the improvement shown by our data depends again on the molecular transport mechanism typical of the pillar geometry and of the superhydrophobic configuration. We also tested a lower concentration of complementary sequences: 1 h exposure to 10 nM provided 30% hybridization on the SAM with a density of 5.4×10^{12} mol/cm^2. In this case the hybridization did not reach the saturation value because of the low concentration, but was still enough to produce a well detectable signal. Similar results were obtained by our group using nanografted oligomer patches;[25] these results were rationalized in term of increased order in the high-density nanografted patches. However, the argument proposed in the present article can also be applied to the case of the nanografted structures. Indeed the size of those structures is even smaller than that of pillars, and the neighboring area was covered with ethylene glycols with an exceptionally low aspecific adsorption. Therefore it is possible to argue that also in that case the process was dominated by spherical adsorption. Both experiments provide a new point of view in modeling DNA hybridization on a surface. In particular we have demonstrated that the probe density itself does not control the hybridization efficiency but for large and flat sensors with increasing probe densities the saturation is reached with exposures that largely exceeds the incubation times used in laboratory experiments.

We believe that our results have important consequences for biosensing applications. In this paper we showed that three-dimensional structures with dimensions comparable to the diffusion length of the target molecules increase the reaction speed by 3 orders of magnitude. However, the same improvement can be found also in concentration sensitivity: in Figure 2, at fixed incubation times the 10 nM solution on pillars produces a larger density than 1 μM solution on flat surfaces. Although we did not focus our attention on the absolute sensitivity of the device, we note that by reducing the size of a factor 10 in all directions our MEMS resonators could detect the adsorption of a single molecule,[12] as already demonstrated in the literature, and can compete with methods based on fluorescence or on electrical transduction. Using 10^n pillars in parallel it will be possible to address concentrations of 10^n below the inverse of the dissociation constant, since there will be always a pillar "occupied" at the equilibrium. Moreover, the detection scheme that we proposed is linear with the number of molecules that bind with the active area, and more in general with the analyte concentration within a large dynamic range, while other methods show strong nonlinearities or reach immediately the saturation.[26−28]

We conclude by emphasizing that the application of pillar sensing to interactomics can be very promising because, as we have already discussed in the introduction and as it is underlined in a recent review article,[1] detection of proteins at an extremely low concentration (below fM) in reasonable time is the challenge of the next generation of biosensors. The goal can be achieved only by a combination of nanotechnologies for improved sensitivity and new geometries to overcome the limitation of slow mass transport by diffusion. We believe that vertical nanomechanical resonators, such as our pillars, arranged in a superhydrophobic device could provide high sensitivity and absolute quantification and will be able to deal with highly diluted solutions. In the future we aim at integrating superhydophobic pillars with microfluidic circuitry in order to perform molecular detection directly in wet environments. Under these conditions the benefit of real time detection would compensate the sensitivity reduction induced by operation in solution. Moreover, matrices of pillars coupled to a scanning readout technique such as the SCALA platform[29] or to a parallel optical detection[30] are intrinsically a flexible platform for multiplexing, since every pillar in the matrix can be functionalized to recognize a different target. For all the reasons listed above, we believe that the approach presented in this paper can represent a valuable starting point for a new sensing paradigm for proteomics.

METHODS

Experimental Setup. The displacement of the pillars at different frequency is measured using the optical deflection method in vacuum. The top of each pillar acts like a tilting mirror (see inset Figure 3). When an illuminated pillar oscillates the reflected light is swung, and its motion is magnified by a factor proportional to the optical path. The light oscillation is detected by a position-sensitive photodiode. The device is placed into a

home-built small vacuum chamber evacuated with a turbo-rotary pump system with base pressure better than 1×10^{-6} mbar. The rotary pump is an oil-free root pump, and the turbo is 70 L/s equipped with magnetic bearings which can be mounted directly on the chamber thus improving evacuation time and base pressure. The rotary pump is mechanically decoupled from the chamber by means of a heavy attenuator. The pressure is constantly monitored with a full scale gauge, because measurements can be compared only if taken under the same conditions due to the dependence on pressure of the mechanical properties of a cantilever.

The optical setup is built using the cage system (from Thorlabs) that consists of a rigid armature of four steel rods, where the optical components are mounted along a common optical axis. The distance between two near rods is 30 mm. The setup serves the purpose to focus a laser beam in a spot of a few micrometers, to focus on a photodetector the light reflected from a pillar, and to visualize by means of a CCD camera the laser spot and the device. The source is a DPSS green laser (532 nm) that can be modulated from 0 to 100 mW ((1) see Figure 3A). A relatively high power is needed because of several reflections along the optical path that reduce the actual power reflected by the pillar on the photodetector. Almost 1/10th of the incident power reaches the pillar surface. We have optimized the optical setup and minimized the power absorbed by the pillar surface to less than 100 μW to reduce the pillar heating induced by the laser. A long working distance microscope objective (2) (LMPLFLN 20X Olympus) with 0.4 numerical aperture and 12 mm working distance focuses the laser to a spot of few micrometers. The diameter of the entrance pupil of the objective is around 7 mm and the beam radius of the laser must be expanded in order to illuminate all the optics of the objective. For this a 10x beam expander (3) is mounted between the laser and the objective. A cubic beamsplitter (4) divides the incident and the reflective light. A tube lens (5), (focal lens 200 mm) is used to correct the infinity focus of the objective. A second beamsplitter (6) serves the purpose to add a white light in optical path for the illumination. The source is a common fiber optic illuminator (7). A mirror, after the tube lens, can direct the light either to the photodetector (8) or to a CCD camera (9) (GANZ ZCF11C4 or THE-IMAGINGSOURCE DBK 41BU02). Alternatively, with a further beamsplitter (10) it is possible to achieve the imaging and the detection at the same time with the drawback to halve the signal on the photodiode. Before the CCD camera a long pass filter (11) (610 nm) stops the laser light allowing only the imaging light to reach the detector, otherwise the laser intensity would saturate the sensor of the camera. The portion of the incident light that passes through the beamsplitter orthogonally with respect to the objective is monitored by a power meter sensor (12).

The optical system is fixed and the scanning over the sample is realized by moving the entire chamber by means of an $x-y$ micrometric translation stage and on a lab jack. A second xyz stage controls the position of the photodetector. Moreover a high precision rotation stage can turn the sensor around the optical axis of the system. The chips are mounted on a chip support made of PEEK with four slots equipped with $3 \times 5 \times 1$ mm³ piezoelectric crystals (lead zirconate titanate) used as actuators. Their capacity ranges from 0.5 to 1.2 nF. The samples are directly glued to the crystals by means of biadhesive tape. We used piezo with both vertical and shear polarization but we did not notice any significant difference in the amplitude of motion of the pillars. This suggests that the direction of vibration of the piezo has a small influence on the motion of a pillar and that the actuation is given by the resonance coupling between the motion of the piezo and the oscillation of pillars.

The photodector is a fast four quadrant photodiode (Hamamatsu S7379-01, cut off frequency ≈ 80 MHz) controlled by dedicated homemade electronics. The signal from the four quadrants is amplified and mixed generating two outputs: the x and y positions of the spot with respect to the center of the photodiode. These values are proportional to the displacement of the illuminated pillar.

A network analyzer (3577A Hewlett–Packard) generates a sweeping signal to excite the piezo and make the pillars to oscillate. Depending on the orientation of the pillars, the vertical or the horizontal signal is acquired by the analyzer which filters the component of the signal at the actuation frequency and provides the amplitude and the phase difference. We always acquired a long series of spectra to avoid initial transient do to local change in the environmental conditions waiting about 20 min until spectra reach a steady state values. This effect is probably due to the evaporation of water that is adsorbed on the pillar either from the ambient humidity or from a direct dipping in a solution. We fit the data with a Lorentzian function whose center x_c and width w give the value of the resonance frequency (x_c) and of the Q-factor (x_c/w).

We measured a single pillar at the time and monitored from three to five pillars in each chip. The range of resonance frequencies is from 4.5 to 8 MHz. The Q factor is around 20000 in vacuum and the responsivity is around 30 Hz/fg. For gold coating we deposited first a layer of titanium (5 nm) and then a layer of gold (15 nm). The rate of deposition was kept low, 0.2 nm/sec, for increasing the uniformity of the metal layer. The mass added is 7.5 ± 0.1 pg.

Materials. The oligonucleotides were purchased from Sigma–Genosys and where used without further purification. The sequences used in the study are as follows:

DNA-target   5′-TAG CCG ATT ACC AAG CCA AGC CAA GCC AAG TAG CCG ATTA-3′

DNA-probe   HS-(CH₂)₆-5′-TAAT CGG CTA CTT GGC TT G GCT TGG CTT GGT AAT CGG CTA-3′

The sequence is designed in order that self-dimerization and hairpin formation are avoided. For this reason the concentration of G or C base, which produces more stable base pair than AT, is limited to 50%. Higher concentration would increase the number of potential self-binding sites.

The other reagents were purchased from Sigma-Aldrich. The DNA solutions were prepared in TE buffer (1 M NaCl, 10 mM Tris, 1 mM EDTA, and pH 7.4) using Milli-Q water (resistivity >18 MΩ·cm). The solution of MCH was prepared in Milli-Q water. Functionalization and hybridization reactions were performed in TE buffer.

After the functionalization and hybridization steps, the samples are successively rinsed in TE buffer, 10 mM phosphate buffered saline (PBS) with Tween 20, 0.05%, and Milli-Q water in order to remove the aspecific DNA adsorption and residual salt from the devices.

Simulation. We carried out finite element simulation (COMSOL) to understand the role of the geometry on the adsorption rate.

We model the behavior of a solution domain (5 mm × 5 mm × 5 mm) at the concentration $c(x,t)$ with the Fick equation.

$$\frac{\partial c}{\partial t} = \nabla \cdot (D \nabla c)$$

At the bottom boundary of the domain there is the adsorbing area. In the case of planar adsorption it corresponds to the entire surface. In the case of the micrometer-sized absorber it is limited to a small rectangle (3 μm × 8 μm) of the 500 μm × 500 μm domain boundary. The local coverage is given by the function $\theta_s(x,t)$ and follows the standard Langmuir equation:

$$\frac{\partial \theta_s}{\partial t} = C_s(t) k_{ads}(\theta_0 - \theta_s(t)) - k_{des}\theta_s$$

where k_{ads} is the rate of adsorption and k_{des} is the rate of desorption. $C_s(t)$ is the solution concentration at the adsorbing area. The adsorption is modeled as an outgoing flux of the concentration so that mass balance gives the coupling between the molecules in solution and the adsorbed molecules.

$$\mathbf{n} \cdot (-D * \nabla c) = -Cs(t) * k_{ads} * (\theta_0 - \theta_s(t)) + k_{des} * \theta_s$$

The software resolves iteratively the two equations, using a pseudo-adiabatic approach. The adsorption time scale is provided by k_{ads} which, in order to reproduce our data, was set to $k_{ads} = 1.32 \times 10^5$ (M·s)$^{-1}$. For the concentrations used in our experiments adsorption time scale ranges from 8 to 800 s. On the other hand the typical diffusion times are slower and range from 100 to 10000 s. Therefore, at each iterative step the diffusion equation can be solved assuming adsorption virtually

instantaneous but the final solution takes into account also the actual adsorption and desorption rates.

At the top boundary the concentration is fixed to a bulk values c_0. At the four lateral boundaries the concentration is let free to change, and the only constraint is that the component of the flux normal to the boundary is set to 0. In the case of the flat sensor, this has the same effect to impose periodic boundaries. In the case of the micrometer-sized sensor the concentration at the boundary remained equal to c_0 and the simulation showed that he depletion region never extends beyond 3 μm from the micrometer-sized surface. Thus the boundary conditions are equivalent to those of an infinite cell. Moreover, the effect of neighboring pillars (which are placed at 20 μm distance) can be neglected. At $t = 0$ the concentration is homogeneous and it is equal to c_0 and the surface coverage is set to 0. After that, the outgoing flux at the active surface depletes a region nearby which generates a gradient of concentration. The main results of these simulations are given in the main text.

REFERENCES AND NOTES

1. Arlett, J. L.; Myers, E. B.; Roukes, M. L. Comparative Advantages of Mechanical Biosensors. *Nat. Nanotechnol.* **2011**, *6*, 203–215.
2. Yang, Y. T.; Callegari, C.; Feng, X. L.; Ekinci, K. L.; Roukes, M. L. Zeptogram-Scale Nanomechanical Mass Sensing. *Nano Lett.* **2006**, *6*, 583–586.
3. von Muhlen, M. G.; Brault, N. D.; Knudsen, S. M.; Jiang, S.; Manalis, S. R. Label-Free Biomarker Sensing in Undiluted Serum with Suspended Microchannel Resonators. *Anal. Chem.* **2010**, *82*, 1905–1910.
4. Squires, T. M.; Messinger, R. J.; Manalis, S. R. Making it Stick: Convection, Reaction and Diffusion in Surface-Based Biosensors. *Nat. Biotechnol.* **2008**, *26*, 417–426.
5. Nair, P. R.; Alam, M. A. Performance Limits of Nanobiosensors. *Appl. Phys. Lett.* **2006**, *88*, 233120.
6. Sheehan, P. E.; Whitman, L. J. Detection Limits for Nanoscale Biosensors. *Nano Lett.* **2005**, *5*, 803–807.
7. Kusnezow, W.; Syagailo, Y. V.; Goychuk, I.; Hoheisel, J. D.; Wild, D. G. Antibody Microarrays: The Crucial Impact of Mass Transport on Assay Kinetics and Sensitivity. *Expert. Rev. Mol. Diagn.* **2006**, *6*, 111–124.
8. Nair, P. R.; Alam, M. A. Screening-Limited Response of NanoBiosensors. *Nano Lett.* **2008**, *8*, 1281–1285.
9. Nair, P. R.; Alam, M. A. Dimensionally Frustrated Diffusion towards Fractal Adsorbers. *Phys. Rev. Lett.* **2007**, *99*, 256101.
10. Kehrbusch, J.; Ilin, E. A.; Hullin, M.; Oesterschulze, E. High Frequency Columnar Silicon Microresonators for Mass Detection. *Appl. Phys. Lett.* **2008**, *93*, 023102.
11. Melli, M.; Pozzato, A.; Lazzarino, M. Inverted Tapered Pillars for Mass Sensing. *Microelectron. Eng.* **2010**, *87*, 730–733.
12. Ilic, B.; Yang, Y.; Aubin, K.; Reichenbach, R.; Krylov, S.; Craighead, H. G. Enumeration of DNA Molecules Bound to a Nanomechanical Oscillator. *Nano Lett.* **2005**, *5*, 925–929.
13. Lafuma, A.; Quere, D. Superhydrophobic States. *Nat. Mater.* **2003**, *2*, 457–460.
14. Wenzel, R. N. Resistance of Solid Surfaces to Wetting by Water. *Ind. Eng. Chem.* **1936**, *28*, 988–994.
15. Cassie, A. B. D.; Baxter, S. Wettability of Porous Surfaces. *Trans. Faraday Soc.* **1944**, *40*, 546.
16. Gentile, F.; Das, G.; Coluccio, M. L.; Mecarini, F.; Accardo, A.; Tirinato, L.; Tallerico, R.; Cojoc, G.; Liberale, C.; Candeloro, P.; *et al.* Ultra Low Concentrated Molecular Detection Using Super Hydrophobic Surface Based Biophotonic Devices. *Microelectron. Eng.* **2010**, *87*, 798–801.
17. Yoshimitsu, Z.; Nakajima, A.; Watanabe, T.; Hashimoto, K. Effects of Surface Structure on the Hydrophobicity and Sliding Behavior of Water Droplets. *Langmuir* **2002**, *18*, 5818–5822.
18. Herne, T. M.; Tarlov, M. J. Characterization of DNA Probes Immobilized on Gold Surfaces. *J. Am. Chem. Soc.* **1997**, *119*, 8916–8920.
19. Georgiadis, R.; Peterlinz, K. P.; Peterson, A. W. Quantitative Measurements and Modeling of Kinetics in Nucleic Acid Monolayer Films Using SPR Spectroscopy. *J. Am. Chem. Soc.* **2000**, *122*, 3166–3173.
20. Peterson, A. W.; Heaton, R. J.; Georgiadis, R. M. The Effect of Surface Probe Density on DNA Hybridization. *Nucleic Acids Res.* **2001**, *29*, 5163–5168.
21. Demers, L. M.; Mirkin, C. A.; Mucic, R. C.; Reynolds, R. A.; Letsinger, R. L.; Elghanian, R.; Viswanadham, G. A Fluorescence-Based Method for Determining the Surface Coverage and Hybridization Efficiency of Thiol-Capped Oligonucleotides Bound to Gold Thin Films and Nanoparticles. *Anal. Chem.* **2000**, *72*, 5535–5541.
22. Gadgil, C.; Yeckel, A.; Derby, J. J.; Hu, W.-S. A Diffusion-Reaction Model for DNA Microarray Assays. *Biotechnology* **2004**, *114*, 31–45.
23. Marie, R.; Jensenius, H.; Thaysen, J.; Christensen, C. B.; Boisen, A. *Ultramicroscopy* **2002**, *91*, 29–36.
24. Alvarez, N. J.; Walker, L. M.; Anna, S. L. Diffusion-Limited Adsorption to a Spherical Geometry: The Impact of Curvature and Competitive Time Scales. *Phys. Rev. E* **2010**, *82*, 011604.
25. Mirmomtaz, E.; Castronovo, M.; Grunwald, C.; Bano, F.; Scaini, D.; Ensafi, A. A.; Scoles, G.; Casalis, L. Quantitative Study of the Effect of Coverage on the Hybridization Efficiency of Surface-Bound DNA Nanostructures. *Nano Lett.* **2008**, *8*, 4134–4139.
26. Zhang, J.; Lang, H. P.; Huber, F.; Bietsch, A.; Grange, W.; Certa, U.; Mckendry, R; Guntherodt, H.-J.; Hegner, M.; Gerber, C. Rapid and Label-Free Nanomechanical Detection of Biomarker Transcripts in Human RNA. *Nat. Nanotechnol.* **2006**, *1*, 214–220.
27. Husale, S.; Persson, H. H. J.; Sahin, O. DNA Nanomechanics Allows Direct Digital Detection of Complementary DNA and MicroRNA Targets. *Nature* **2009**, *462*, 1075–1078.
28. Hahm, J.; Lieber, C. M. Direct Ultrasensitive Electrical Detection of DNA and DNA Sequence Variations Using Nanowire Nanosensors. *Nano Lett.* **2004**, *4*, 51–54.
29. Kosaka, P. M.; Tamayo, J.; Gil-Santos, E.; Mertens, J.; Pini, V.; Martínez, N. F.; Ahumada, O.; Calleja, M. J. Simultaneous Imaging of the Topography and Dynamic Properties of Nanomechanical Systems by Optical Beam Deflection Microscopy. *Appl. Phys.* **2011**, *109*, 064315.
30. Sampathkumar, A.; Ekinci, K. L.; Murray, T. W. Multiplexed Optical Operation of Distributed Nanoelectromechanical Systems Arrays. *Nano Lett.* **2011**, *11*, 1014–1019.
31. Steel, A. B.; Levicky, R. L.; Herne, T. M.; Tarlov, M. J. Immobilization of Nucleic Acids at Solid Surfaces: Effect of Oligonucleotide Length on Layer Assembly. *Biophys. J.* **2000**, *79*, 975–981.